Energy Advances

ROYAL SOCIETY OF CHEMISTRY

PAPER

View Article Online
View Journal | View Issue

Cite this: *Energy Adv.*, 2025, 4, 1356

Attaining a fast-conducting, hybrid solid state separator for all solid-state batteries through a facile wet infiltration method

Philip Heuer,[a] Lukas Ketter,[ab] Moumita Rana,[c] Felix Scharf,[d] Gunther Brunklaus[d] and Wolfgang G. Zeier[*ad]

Received 23rd May 2025,
Accepted 2nd September 2025

DOI: 10.1039/d5ya00141b

rsc.li/energy-advances

Thin, fast-conducting and mechanically robust separators are expected to be advantageous in enabling all-solid-state batteries with high energy densities and good electrochemical performance. In this study, a potentially new scalable fabrication route for flexible thiophosphate–polymer separator membranes is demonstrated. By infiltrating a commercially available polymer mesh with the highly conductive inorganic solid ion conductor $Li_{5.5}PS_{4.5}Cl_{1.5}$, a hybrid separator membrane with a high ionic conductivity is realized. The electrochemical evaluation *via* rate capability tests reveals superior performance at low stack pressures and high C-rates, when comparing cells employing the hybrid membrane separator, to cells utilizing conventional solid electrolyte separators. As a proof of concept, a full cell implementing the hybrid membrane between a Si-based anode and a $LiNi_{0.83}Co_{0.11}Mn_{0.06}O_2$–$Li_{5.5}PS_{4.5}Cl_{1.5}$ composite cathode is evaluated. The experimental work is complemented by resistor network modelling of the hybrid membrane sheets, shedding light on potential challenges in cell operation.

Introduction

Lithium-ion batteries are the most widely used electrochemical energy storage systems for portable electronic devices today. However, the lithium-ion technology slowly reaches its theoretical limits in terms of energy density, and the need for alternatives is greater than ever, due to the increasing energy demand of our society.[1,2] All-solid-state batteries could be a promising next generation technology offering both higher energy density and improved safety. While the replacement of the liquid electrolyte with a solid electrolyte paves the way for high energy electrodes[2] on the one hand, safety aspects such as leakage or flammability of the electrolyte may become obsolete on the other.[3] Although all-solid-state batteries are promising, the technology is challenging and fundamental questions in terms of processability, scalability, and physical and electrochemical properties of the solid electrolyte remain unclear. In addition, high costs due to under-developed infrastructure for large-scale production or the handling of Li-metal negative electrodes still need to be evaluated and tested for their practicability.[4]

Since the implementation of lithium as a metal anode in solid-state batteries still presents several challenges, such as dendrite growth or continuous SE degradation due to unfavorable SEI formation, Si/C is emerging as an alternative focus in many studies.[5–7] Silicon has an inherently high and promising theoretical capacity of approximately 3579 mAh g^{-1},[8] but during the lithium insertion and extraction processes, it undergoes significant volume changes of up to 300%,[9] resulting in reduced electronic percolation, irreversible lithium trapping, and capacity loss, among others.[10] To address this issue, the use of carbon additives is a common method that effectively buffers the volume changes while preserving electronic percolation.[11] To compete with current lithium-ion batteries, solid-state batteries need to reach higher power and energy densities. First, this is possible with higher active material loadings whereby fast ion conductors are key to reducing the inherent transport limitations in solid-state electrode composites.[12] A promising solid electrolyte class exhibiting high ionic conductivities is thiophosphates, with Li-argyrodites such as Li_6PS_5Cl or $Li_{5.5}PS_{4.5}Cl_{1.5}$ standing out due to their mechanical and electrochemical properties, among other sulfidic electrolytes.[13,14]>

Second, an increase in the energy density of the solid state battery can be realized when the resistance of the solid electrolyte separator is reduced.[15,16] While fast ion-conductors can

[a] *Institute of Inorganic and Analytical Chemistry, University of Muenster, Corrensstrasse 28/30, 48149 Muenster, Germany. E-mail: wzeier@uni-muenster.de*
[b] *International Graduate School of Battery Chemistry, Characterization, Analysis, Recycling and Application (BACCARA), University of Muenster, Muenster 48149, Germany*
[c] *Electrical Sustainable Energy Department, Electrical Engineering, Mathematics & Computer Science, Delft University of Technology, Mekelweg 4, 2628 CD Delft, Netherlands*
[d] *Institute of Energy Materials and Devices (IMD), IMD-4: Helmholtz-Institut Muenster, Forschungszentrum Juelich, 48149 Muenster, Germany*

also be a solution, reduction of the separator thickness should be the direction to achieve the goal. As an example, the need for a thin separator was demonstrated by Lee *et al.*, where a 30 μm thick separator was introduced, leading to energy densities of 900 Wh L^{-1}.[17] However, film preparation of solid electrolyte separators requires the use of complicated binder and solvent mixtures.[18] One promising alternative strategy is to combine polymers with inorganic sulfide solid electrolytes *via* a hybrid approach.[19] For instance, Kim *et al.*[20] recently showed that combining a polymeric membrane of 45 μm size with a sulfide solid electrolyte can enhance the physical contact between the separator and electrodes, thus improving cell performance, when compared to a reference cell without the polymer.

Motivated by the promising approach of combining a polymeric membrane with a sulfide solid electrolyte that exhibits a high ionic conductivity, a proof-of-concept approach for the use of a commercial polyamide membrane (nylon 6.6) as the framework for a flexible and free-standing separator is explored in this work. By using an infiltration technique (Fig. 1(a)), the polyamide mesh may help to easily create and upscale a thin, flexible, and fast-conducting membrane as shown in Fig. 1. After the fabrication and characterization of the free-standing membrane itself, it is tested as a separator in half-cells and solid-state battery full cells. This work shows that already existing fast and easy processes can be used to produce thin, flexible, and highly ion-conducting separators with promising cell performance.

Results and discussion

$Li_{5.5}PS_{4.5}Cl_{1.5}$ ($LPSCl_{1.5}$) was chosen as the solid electrolyte because of its high ionic conductivity of ~10 mS cm^{-1} [21] and good performance in solid-state batteries.[22] A commercially available nylon 6.6 mesh (Fig. 2(a)) was used as a three-dimensional scaffold for infiltration. Its high thermal and mechanical[23] stability makes it an ideal component for hybrid membrane preparation. Besides the nylon 6.6 mesh, alternative scaffold materials (polyaramid (Kevlar) and polyethylene (PE)) were also investigated. However, the resulting hybrid membranes were found to be less suitable and the results are discussed in Section S1 of the SI. In addition, grafted cyclodextrin–polycaprolactone (GCD–PCL)[24] was used as a binder to improve the flexibility. Polycaprolactone based polymers are well compatible with argyrodite and are characterized by good wettability toward inorganic particles and electrodes. In addition, GCD–PCL's electrochemical stability window of >4.5 V allows the use of higher voltage cathode materials such as $LiNi_{0.83}Co_{0.11}Mn_{0.06}O_2$ (NCM_{83}).[24,25] The chosen solvent is *p*-xylene, as sulfide solid electrolytes have shown good stability against it.[26] To ensure that the solid electrolyte is not detrimentally affected by the solvent procedure, comparison measurements of X-ray diffraction, Raman and impedance spectroscopy were performed before and after the *p*-xylene treatment (Fig. S4). Scanning electron micrographs of the polymer scaffold and the infiltrated hybrid membrane are shown in Fig. 2. A comparison of hybrid membranes with and without the binder are shown in Fig. S5. It is apparent that the solid electrolyte particles are more strongly adhered to each other when a binding agent is used. Moreover, physical handling of the sheets after infiltration is complicated, as cracks appear and solid electrolyte particles easily detach from the hybrid membrane when no binder is used. Additionally, the thickness of the infiltrated layer can be well controlled by adjusting the amount of dispersion. With the appropriate amount, the infiltration primarily fills the pores of the mesh, and only a small amount of $LPSCl_{1.5}$ accumulates on the surface connecting the pores with each other. The false-colored image section in Fig. 2(b) (energy dispersive spectral maps shown in Fig. S5) further shows the elemental distribution of C and S and highlights that the pores of the polymer framework are interconnected by the solid electrolyte matrix of $LPSCl_{1.5}$.

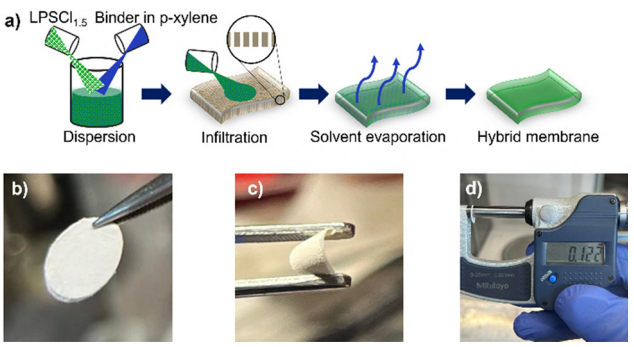

Fig. 1 (a) Schematic illustration of the membrane preparation. Photographs showing (b) an infiltrated membrane, (c) a bent, infiltrated membrane, and (d) thickness measurement, showing the membrane thickness in mm.

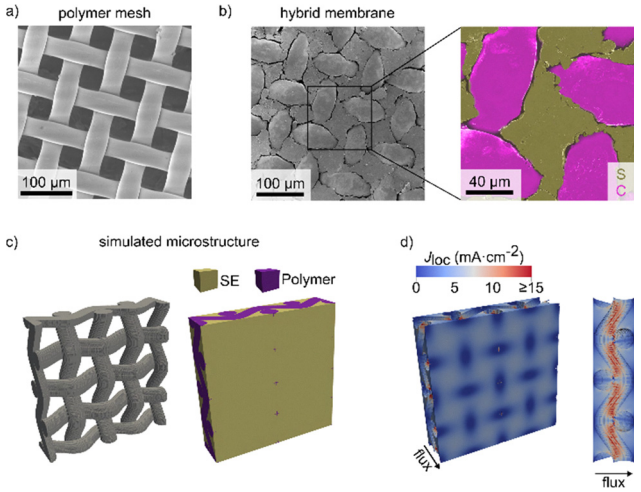

Fig. 2 Scanning electron micrographs of (a) empty and (b) infiltrated PA membranes with the binder and a false-colored image section showing the distribution of S and C. (c) Simulated microstructure of the polymer scaffold and the SE–polymer composite. The composite structure consists of 100 × 400 × 400 voxels, with each voxel representing a volume of 1 $μm^3$. (d) Local current densities (J_{loc}) flowing through the solid electrolyte phase when applying a virtual potential gradient of 0.01 V to the system.

Another important aspect is the presence of continuous ion transport from the top to bottom. Cross-sectional SEM images (Fig. S6), show that $LPSCl_{1.5}$ fills the pores of the polymer scaffold and forms continuous ion conducting pathways. Inserting an obstacle into a conductive phase inevitably leads to a reduction in conductivity.[27] To study this effect on ionic transport, when embedding a polymer mesh into a SE matrix, transport simulations have been performed. First, a virtual mesh microstructure was constructed (Fig. S7) based on the scanning electron micrographs (SEM) and the details of the mesh provided from the manufacturer (Fig. 2(c)). After filling the virtual mesh structure with a second phase describing the solid electrolyte, a virtual composite consisting of ~60 vol% solid electrolyte and ~40 vol% polymer phase was generated. As isolating boundary conditions were assumed in the model, simulations were carried out on composites of different sizes to exclude boundary effects (polymer phases shown in Fig. S8). By specifying the ionic conductivities of both the insulating polymer ($\sigma_{ion,polymer} \approx 0$ mS cm^{-1})[28] and the solid electrolyte phase after solvent treatment ($\sigma_{ion,LPSCl_{1.5}} = 7.1$ mS cm^{-1}) and then performing a resistor network simulation as described previously,[29] the effective ionic conductivity of the virtual composite was computed, yielding $\sigma_{ion,composite} = 3.3$ mS cm^{-1}. This value corresponds to a reduction to slightly less than half the conductivity of the pure solid electrolyte and can be viewed as the upper conductivity limit, given that the mesh structure is perfectly packed with solid electrolytes in the simulations. In addition to the average ionic transport in the mesh membrane, the local flux densities flowing through each node of the resistor network were calculated from the stationary potential distribution using Ohm's law (Fig. 2(d)). The result indicates that the mesh structure may cause an uneven ion current density distribution and current constriction at the interface with the electrodes. This may potentially impair the performance, especially when metal electrodes are used.[30,31] To systematically study the effects of both interfacial porosity and pore depth on the effective ionic conductivity, the solid electrolyte phase near the interface was partially replaced by pores ($\sigma_{pore} = 0$ mS cm^{-1}) generated using the blobs function from the PoreSpy library[32] (Fig. 3(a)). A total of 16 simulations were conducted, varying the porosity between 20% and 80% and the pore depth between 5 μm and 20 μm. Top-view images of the resulting virtual microstructures are presented in Fig. 3(b). Among these, structures with higher porosity (≥60%) and greater pore depth (≥15 μm) exhibited the closest visual agreement with the measured SEM images (Fig. 2(b)). The corresponding simulated effective ionic conductivities are shown in Fig. 3(c), demonstrating that both increasing pore depth and interface porosity lead to an overall decrease in effective conductivity. Notably, within the investigated ranges, the impact of interface porosity on the effective conductivity is more pronounced than that of pore depth. Furthermore, high interface porosities and pore depths can strongly decrease the effective ionic conductivity to below 1.0 mS cm^{-1}.

In addition to the simulations, temperature-dependent electrochemical impedance spectroscopy was used to study the

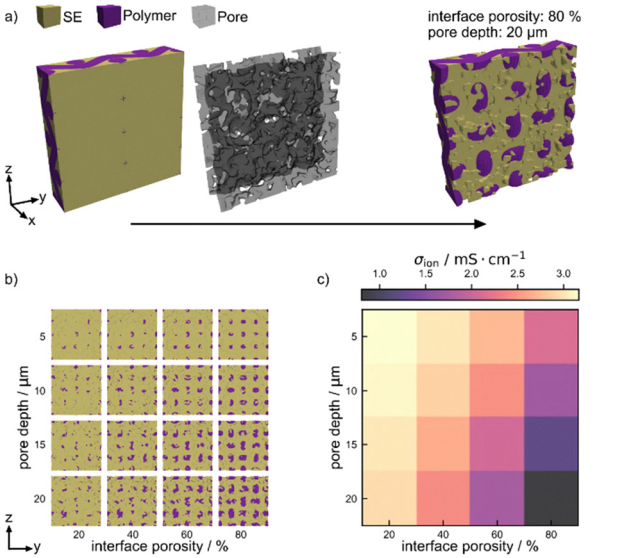

Fig. 3 (a) Introduction of interfacial porosity into the virtual microstructure. (b) Top-view images of the virtual microstructures with varying pore depths and interface porosity. (c) Ionic conductivity as a function of pore depth and interface porosity for the infiltrated mesh structure.

effective ionic conductivity of the infiltrated mesh structure. Representative Nyquist plots are shown in the SI (Fig. S9) and the corresponding Arrhenius plots for the pristine $LPSCl_{1.5}$ and hybrid membranes are shown in Fig. 4(a). The room temperature ionic conductivity was determined using an equivalent circuit consisting of a resistor and a constant phase element in series. An overall decrease of the ionic conductivity from 8.3 mS cm^{-1} (pristine $LPSCl_{1.5}$) to 7.1 mS cm^{-1} ($LPSCl_{1.5}$ after solvent treatment) to 0.9 mS cm^{-1} ($LPSCl_{1.5}$@GCD–PCL@PA, 140 μm) is observed. The measured conductivity of the hybrid membrane lies below the calculated upper conductivity limit. While the solvent treatment has only little impact on the ionic conductivity (Fig. S4c), the observed mismatch in simulated and measured conductivity is likely due to poor contact between the hybrid membrane and the current collectors during impedance measurements (Fig. 3c), as well as the presence of pores between the polymer scaffold and the solid electrolyte. In an additional experiment, improved interfacial contact was achieved by applying excess $LPSCl_{1.5}$ on both sides of the separator, which yielded an increased measured conductivity of 2 mS cm^{-1} (Section 5 of the SI).

The linear behavior of the Arrhenius data (Fig. 4(a)) across the whole temperature range indicates no side phase formation after the infiltration process with *p*-xylene as no significant change in the activation energy of ion transport before and after infiltration is observed (0.40 eV and 0.42 eV). This indicates that lithium-ion transport remains unaffected, with the mesh serving solely as a mechanical stabilizing framework.

To further explore the electrochemical properties of the hybrid membrane, we measured them in a half-cell configuration. We employed the $NCM_{83}/LPSCl_{1.5}$ composite in a weight ratio of (70 : 30) as the positive electrode and Li/In alloy as the counter electrode. As a reference, half-cells were built with a

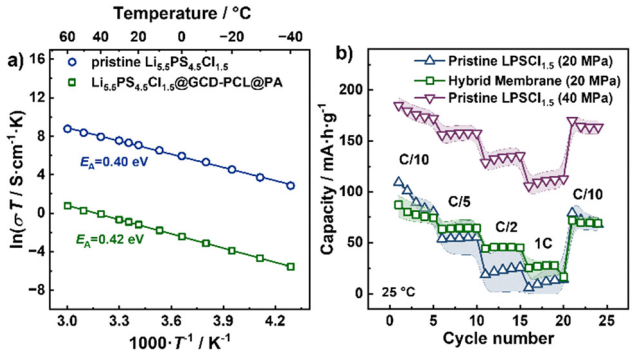

Fig. 4 (a) Arrhenius plot of the infiltrated membrane $LPSCl_{1.5}$@GCD–PCL@PA with activation energy E_A = 0.42 eV and pristine $LPSCl_{1.5}$ with activation energy E_A = 0.40 eV. (b) Discharge capacities of the rate-performance test in a Li/In half-cell setup at 20 MPa and 40 MPa, where 1C = 180 mAh g^{-1}.

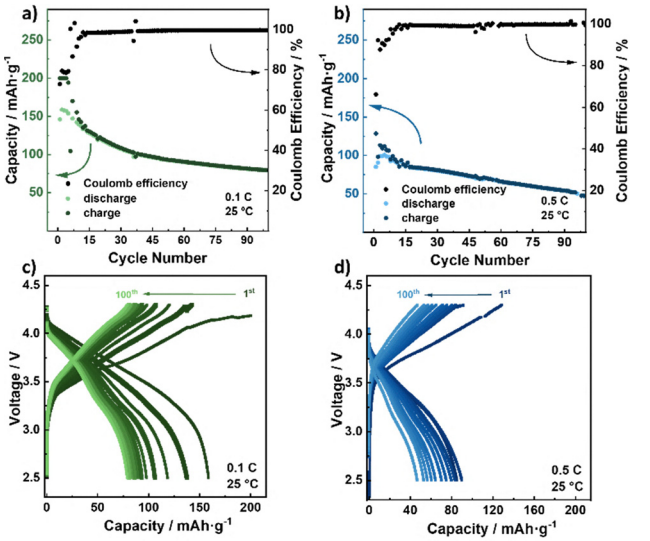

Fig. 5 Full cell performance of $LPSCl_{1.5}$@GCD–PCL@PA in the potential range from 2.6 V to 4.3 V at 25 °C, a pressure of 50 MPa and a current density of 0.18 mA cm^{-2} (0.1C) and 0.90 mA cm^{-2} (0.5C). A 70 wt% : 30 wt% mixture of NCM_{83} and $LPSCl_{1.5}$ was used as the cathode composite. The anode composite was a mixture of Si/C and $LPSCl_{1.5}$ in a weight ratio of 55 : 45. (a) and (b) Capacity retention and Coulomb efficiency over 100 cycles at 0.1C and 0.5C. (c) and (d) Charge and discharge curves for every 10th cycle (1st, 10th, ..., 100th) at 0.1 and 0.5C.

9wtypical 600 μm thick pristine $LPSCl_{1.5}$ separator.[33] As reported previously, the performance of all-solid-state batteries is highly sensitive to applied stack pressure during the measurement,[33,34] and Fig. 4(b) also shows that a decrease in the stack pressure from 40 MPa to 20 MPa causes a significant decrease in the specific capacity of the electrode at different C-rates (Fig. 4(b)). Note that the thin hybrid membrane applying a pressure of 40 MPa was not possible. By applying a stack pressure of 20 MPa, we prevent the metal anode from penetrating the relatively thin membrane, which would cause the cell to short-circuit directly after assembly. When the hybrid membrane is used as the separator, the specific capacity values at different current densities are comparatively more stable compared to the one with a compressed pristine $LPSCl_{1.5}$ separator. Considering the lower stack pressure of 20 MPa, the cell with the hybrid membrane shows an adequate discharge capacity of 78 (±9) mAh g^{-1} at 0.1C and better performance compared to the fully inorganic cell at elevated C-rates. While the fully inorganic cell initially exhibits higher discharge capacities at C/10, its performance converges with that of the hybrid cell after approximately five cycles. Toward the end of the measurement, both cells show comparable cycling behavior at C/10. The discharge capacity for the hybrid membrane at 0.2C is 64 (±6) mAh g^{-1}, whereas the value of 54 (± 15) mAh g^{-1} for the pristine $LPSCl_{1.5}$ is already lower. This gap increased at 0.5 and 1C, and the observed capacities for the hybrid membrane are still 46 (±1) mAh g^{-1} and 28 (±8) mAh g^{-1}, respectively.

Since these results are quite promising as a proof of concept, a full cell with a Si/C composite as the anode and the previously mentioned NCM_{83} composite cathode is built, and the corresponding cell setup and experimental conditions are shown in Fig. S10. Using a composite containing Si/C instead of a Li/In alloy enables the cell to cycle at 50 MPa without the risk of Li/In penetrating the membrane. A N/P ratio of unity was selected. To examine whether the current density influences the long-term cycling behavior, the full cells were cycled at 0.1C and 0.5C. Fig. 5(a) and (b) show that after 15 formation cycles, the discrepancy between charge and discharge capacity has equalized. After 100 cycles, a capacity retention of 60% at 0.1C and 55% at 0.5C is observed. The Coulomb efficiency increases to >99.5% after 50 cycles and is somewhat more stable for the cell cycled at 0.1C. The first, 25th, 50th, and 100th charge and discharge profiles at 0.1C and 0.5C are shown in Fig. 5(c) and (d). A noticeable capacity loss for the cell cycled at 0.1C was observed within the first 25 cycles. This behavior can be attributed to the formation of SEI and CEI, which may consume active lithium under slow cycling conditions.[35] For the full cell cycled at 0.5C, a larger capacity loss is observed between cycles 50 and 100. This may be due to the inherently higher rate leading to reduced performance right from the beginning. The faster cycling rate tends to stress the system more than the slower rate, resulting in greater capacity fade over time.[36]

Experimental section

Synthesis

The synthesis route for $Li_{5.5}PS_{4.5}Cl_{1.5}$ ($LPSCl_{1.5}$) has been previously reported.[37] All synthesis procedures and sample treatment for $LPSCl_{1.5}$ were performed under an argon atmosphere (<0.5 ppm H_2O and O_2). Lithium sulfide (Li_2S, Alfa-Aesar, 99.9%), phosphorus pentasulfide (P_2S_5, Merck, 99%), and lithium chloride (LiCl, Alfa-Aesar, 99.9%) were hand ground for 15 minutes to obtain 3 g batches. The mixed materials were then hand pressed into pellets and filled into 8 cm high silica ampoules. The ampoules were prepared with a carbon coating and preheated at 800 °C for 2 h under vacuum to remove all residual moisture. After placing the precursor in the ampoules,

the ampoules were sealed under vacuum. After 3 days of heating at 450 °C (ramp rate: 100 °C h^{-1}, natural cooling), the powders were ground for 15 min, followed by the repetition of pelletizing, sealing inside the prepared ampoule and annealing of the sample at 450 °C (ramp rate: 100 °C h^{-1}, natural cooling) for additional 3 days.

Membrane preparation

The membrane preparation was performed inside an Ar filled glovebox (<0.5 ppm H_2O and O_2). The slurry was mixed by stirring 400 mg $LPSCl_{1.5}$ and 30 mg of grafted cyclodextrin–polycaprolactone[38] for 1 h in 5 ml *p*-xylene (Thermo Fisher, <0.05% H_2O, >99% purity) on a stirring plate. A self-designed infiltration tool was used for membrane preparation (Fig. S1). A pre-dried membrane (radius = 4.5 mm, thickness = 100 μm) and 0.5 ml of the slurry were used to prepare a 140 μm thick $LPSCL_{1.5}$@GCD–PCL@PA membrane. The still wet membrane was then transferred into a Büchi oven and dried at 80 °C for 60 h under dynamic vacuum. Before using the membrane, it was compressed uniaxially at 375 MPa for 3 min. The comparison solvent treatment was performed by stirring a 20 wt% dispersion of $LPSCl_{1.5}$ and *p*-xylene for 1 h. The solvent was then evaporated under dynamic vacuum at 80 °C overnight.

Powder X-ray diffraction

Powder X-ray diffraction was performed using a StadiP from STOE in Debye–Scherrer geometry with Cu-K_α radiation (λ = 1.5451 Å). $LPSCl_{1.5}$ was sealed in 0.5 mm borosilicate capillaries and measured at 2θ steps of 3° for 120 s in the 2θ range of 10°–91°.

Raman spectroscopy

The obtained powder of $LPSCl_{1.5}$, solvent-treated $LPSCl_{1.5}$ and infiltrated membranes were placed on a Raman sample holder, which were closed airtight to prevent the samples from side reactions and humidity. The measurements were performed using a Bruker Senterra II and a 532 nm laser source.

Field emission scanning electron microscopy and energy dispersive X-ray spectroscopy

Scanning electron micrographs (SEM) were collected using a Carl Zeiss AURIGA CrossBeam working station and an accelerating voltage of 3 kV. For the energy dispersive (EDX) measurement, an 80 mm^2 X-Max detector at an acceleration voltage of 15 kV was used.

Electrochemical cell assembly

All electrochemical measurements were carried out in PEEK lined, airtight press cells with stainless steel current collectors (A = 0.785 cm^2).[39] All measurements were performed using a Biologic-VMP300 and a climate chamber maintained at 25 °C.

For electrochemical impedance spectroscopy, 100 mg of $Li_{5.5}PS_{4.5}Cl_{1.5}$ or an infiltrated membrane was placed in between two steel stamps and uniaxially pressed at 375 MPa for 3 min. An external pressure of 50 MPa was then applied using a metal frame. The frequency range for impedance measurements was 1 MHz to 100 mHz. RelaxIs software (rhd instruments) was used for the analyses.

For the full cell, an anode composite and a cathode composite were mixed with a shaker mill (Fritsch, Pulversiette 23) at 45 Hz for 10 min. 100 mg of the cathode composite was prepared by mixing 70 wt% $LiNi_{0.83}Co_{0.11}Mn_{0.06}O_2$ (MSE Supplies) and 30 wt% $LPSCl_{1.5}$. NCM_{83} was dried at 250 °C overnight under dynamic vacuum in a B-585 oven. The anode composite consisted of Si/C powder (10 wt% Si, 90 wt% C) and $LPSCl_{1.5}$ in a ratio of 55 wt% to 45 wt%.[11] To build the cell with a N/P ratio of 1, 12 mg of the cathode composite (mass loading: 10.7 mg cm^{-2}) was distributed on one of the steel stamps and pressed together with the separator at 375 MPa for 3 min. Then, 5.8 mg of the anode composite was homogeneously distributed on the other side of the separator and pressed by hand. The long-term stability tests were conducted at C/2 for 140 and at C/10 for 100 cycles in a voltage window of 2.6–4.3 V.

For the half-cell setup, the cathode composite was retained but instead of the anode composite 1.5 mg of Li (abcr, 99.8%) and a 9 mm In-foil (chemPUR, 100 μm thickness, 99.99%) were pressed onto the other steel stamp. Rate performance was measured 5 times at C/10 (j = 0.214 mA cm^{-2}), C/5 (j = 0.428 mA cm^{-2}), C/2 (j = 1.070 mA cm^{-2}), C/1 (j = 2.140 mA cm^{-2}), and finally measured again at C/10. The voltage window was 2.0–3.7 V *versus* In/LiIn. We selected the maximum pressure under which stable cycling of the half-cell could still be achieved without inducing mechanical failure or short-circuit. All electrochemical measurements were thus carried out at a stack pressure of 20 MPa.

Conclusions

This work demonstrates a successful infiltration of a polyamide mesh using $Li_{5.5}PS_{4.5}Cl_{1.5}$ and a polycaprolactone based polymer as a binder. The whole process of membrane preparation including infiltration, drying and cold pressing is simple and can be easily optimized for instance by introducing calendaring or hot-pressing steps. The ionic conductivity of 0.9 mS cm^{-1} is reasonably high and will not be the limiting factor as a separator for high performance solid-state batteries. Nevertheless, simulations of the transport in these hybrid sheets suggest potential current constrictions at high current densities. The successful incorporation of the hybrid membrane into a solid-state battery full cell has been achieved *via* a proof-of-concept approach. Overall, the development of a fast-conducting hybrid membrane that can be used as a separator in solid-state batteries is possible using simple techniques. With minor improvements, they can achieve similar electrochemical performance to their nonhybrid competitors. Nevertheless, open questions regarding dendrite penetration and potential current constrictions remain, which may make this concept useful only when composite electrodes are used in both the anode and cathode.

Author contributions

The manuscript was written through contributions of all authors. All authors have given approval to the final version of the manuscript. P. H.: conceptualization, experimental investigation, formal analysis, writing, visualization. L. K.: data evaluation, writing – review and editing. M. R.: writing – review and editing, supervision. F. S.: resources, writing – review and editing. G. B.: resources, writing – editing and review. W. G. Z.: conceptualization, resources, writing – review and editing, supervision.

Conflicts of interest

There are no conflicts to declare.

Data availability

All datasets analysed during this study can be accessed *via* **https://doi.org/10.17879/72998444586** and are provided by the University of Münster's datastore.

Supplementary information: Detailed description of the infiltration tool used for hybrid membrane fabrication, as well as a trial-and-error section outlining different membrane and infiltration strategies and issues encountered during cell assembly and testing. It also provides information on the solvent treatment on the LPSCl1.5, additional SEM and EDX measurements, computational details, electrochemical impedance analysis, and the full-cell setup. See DOI: **https://doi.org/10.1039/d5ya00141b**.

Acknowledgements

We thank Elina Nazmutdinova for support in the SEM measurements. The simulations for this work were carried out on the computer cluster PALMA II at the University of Muenster. The research was supported by the Federal Ministry for Research, Technology and Aeronautics (BMFTR) within the project FESTBATT under grant number 03XP0428F. We further acknowledge the funding from the Deutsche Forschungsgemeinschaft under project number 459785385.

References

1 J. Janek and W. G. Zeier, *Nat. Energy*, 2023, **8**, 230–240.
2 J. Janek and W. G. Zeier, *Nat. Energy*, 2016, **1**, 16141.
3 X. Yu, R. Chen, L. Gan, H. Li and L. Chen, *Engineering*, 2023, **21**, 9–14.
4 L. Mauler, F. Duffner, W. G. Zeier and J. Leker, *Energy Environ. Sci.*, 2021, **14**, 4712–4739.
5 H. Huo and J. Janek, *ACS Energy Lett.*, 2022, **7**, 4005–4016.
6 A. Song, W. Zhang, H. Guo, L. Dong, T. Jin, C. Shen and K. Xie, *Adv. Energy Mater.*, 2023, **13**, 2301464.
7 Y. Huang, B. Shao, Y. Wang and F. Han, *Energy Environ. Sci.*, 2023, **16**, 1569–1580.
8 D. H. S. Tan, Y.-T. Chen, H. Yang, W. Bao, B. Sreenarayanan, J.-M. Doux, W. Li, B. Lu, S.-Y. Ham, B. Sayahpour, J. Scharf, E. A. Wu, G. Deysher, H. E. Han, H. J. Hah, H. Jeong, J. B. Lee, Z. Chen and Y. S. Meng, *Science*, 2021, **373**, 1494–1499.
9 Y. Yang, W. Yuan, W. Kang, Y. Ye, Q. Pan, X. Zhang, Y. Ke, C. Wang, Z. Qiu and Y. Tang, *Sustainable Energy Fuels*, 2020, **4**, 1577–1594.
10 F. Lindgren, D. Rehnlund, R. Pan, J. Pettersson, R. Younesi, C. Xu, T. Gustafsson, K. Edström and L. Nyholm, *Adv. Energy Mater.*, 2019, **9**, 1901608.
11 Y. Rudel, M. Rana, J. Ruhl, C. Rosenbach, J. Müller, P. Michalowski, A. Kwade and W. G. Zeier, *Batteries Supercaps*, 2023, **6**, 1–6.
12 P. Minnmann, L. Quillman, S. Burkhardt, F. H. Richter and J. Janek, *J. Electrochem. Soc.*, 2021, **168**, 040537.
13 L. Peng, C. Yu, S. Cheng and J. Xie, *Batteries Supercaps*, 2023, **6**, e202200553.
14 X. Bai, Y. Duan, W. Zhuang, R. Yang and J. Wang, *J. Mater. Chem. A*, 2020, **8**, 25663–25686.
15 S. Ohno and W. G. Zeier, *Acc. Mater. Res.*, 2021, **2**, 869–880.
16 S. Randau, D. A. Weber, O. Kötz, R. Koerver, P. Braun, A. Weber, E. Ivers-Tiffée, T. Adermann, J. Kulisch, W. G. Zeier, F. H. Richter and J. Janek, *Nat. Energy*, 2020, **5**, 259–270.
17 Y.-G. Lee, S. Fujiki, C. Jung, N. Suzuki, N. Yashiro, R. Omoda, D.-S. Ko, T. Shiratsuchi, T. Sugimoto, S. Ryu, J. H. Ku, T. Watanabe, Y. Park, Y. Aihara, D. Im and I. T. Han, *Nat. Energy*, 2020, **5**, 299–308.
18 H. El-Shinawi, E. Darnbrough, J. Perera, I. McClelland, D. E. J. Armstrong, E. J. Cussen and S. A. Cussen, *ACS Appl. Mater. Interfaces*, 2023, **15**, 36512–36518.
19 H. M. Woolley and N. M. Vargas-Barbosa, *J. Mater. Chem. A*, 2023, **11**, 1083–1097.
20 D. Kim, H. Lee, Y. Roh, J. Lee, J. Song, C. B. Dzakpasu, S. H. Kang, J. Choi, D. H. Kim, H. J. Hah, K. Y. Cho, Y. Lee and Y. M. Lee, *Adv. Energy Mater.*, 2024, **14**, 2302596.
21 C. Yu, F. Zhao, J. Luo, L. Zhang and X. Sun, *Nano Energy*, 2021, **83**, 105858.
22 M. Rana, Y. Rudel, P. Heuer, E. Schlautmann, C. Rosenbach, M. Y. Ali, H. Wiggers, A. Bielefeld and W. G. Zeier, *ACS Energy Lett.*, 2023, **8**, 3196–3203.
23 F. Chavarria and D. R. Paul, *Polymer*, 2004, **45**, 8501–8515.
24 Y. Chen, P. Lennartz, K. L. Liu, Y. Hsieh, F. Scharf, R. Guerdelli, A. Buchheit, M. Grünebaum, F. Kempe, M. Winter and G. Brunklaus, *Adv. Funct. Mater.*, 2023, **33**, 2300501.
25 F. Scharf, A. Krude, P. Lennartz, M. Clausnitzer, G. Shukla, A. Buchheit, F. Kempe, D. Diddens, P. Glomb, M. M. Mitchell, T. Danner, A. Heuer, A. Latz, M. Winter and G. Brunklaus, *Small*, 2024, **20**, 1–14.
26 K. T. Kim, T. Y. Kwon and Y. S. Jung, *Curr. Opin. Electrochem.*, 2022, **34**, 101026.
27 B. Tjaden, S. J. Cooper, D. J. Brett, D. Kramer and P. R. Shearing, *Curr. Opin. Chem. Eng.*, 2016, **12**, 44–51.
28 J. A. Heiser, J. A. King, J. P. Konell and L. L. Sutter, *Adv. Polym. Technol.*, 2004, **23**, 135–146.

29 L. Ketter, N. Greb, T. Bernges and W. G. Zeier, *Nat. Commun.*, 2025, **16**, 1411.
30 X. Zhang, Q. J. Wang, K. L. Harrison, S. A. Roberts and S. J. Harris, *Cell Rep. Phys. Sci.*, 2020, **1**, 100012.
31 T. Krauskopf, B. Mogwitz, C. Rosenbach, W. G. Zeier and J. Janek, *Adv. Energy Mater.*, 2019, **9**, 1902568.
32 J. Gostick, Z. Khan, T. Tranter, M. Kok, M. Agnaou, M. Sadeghi and R. Jervis, *J. Open Source Softw.*, 2019, **4**, 1296.
33 S. Puls, E. Nazmutdinova, F. Kalyk, H. M. Woolley, J. F. Thomsen, Z. Cheng, A. Fauchier-Magnan, A. Gautam, M. Gockeln, S.-Y. Ham, M. T. Hasan, M.-G. Jeong, D. Hiraoka, J. S. Kim, T. Kutsch, B. Lelotte, P. Minnmann, V. Miß, K. Motohashi, D. L. Nelson, F. Ooms, F. Piccolo, C. Plank, M. Rosner, S. E. Sandoval, E. Schlautmann, R. Schuster, D. Spencer-Jolly, Y. Sun, B. S. Vishnugopi, R. Zhang, H. Zheng, P. Adelhelm, T. Brezesinski, P. G. Bruce, M. Danzer, M. El Kazzi, H. Gasteiger, K. B. Hatzell, A. Hayashi, F. Hippauf, J. Janek, Y. S. Jung, M. T. McDowell, Y. S. Meng, P. P. Mukherjee, S. Ohno, B. Roling, A. Sakuda, J. Schwenzel, X. Sun, C. Villevieille, M. Wagemaker, W. G. Zeier and N. M. Vargas-Barbosa, *Nat. Energy*, 2024, **9**, 1310–1320.
34 J. M. Doux, Y. Yang, D. H. S. Tan, H. Nguyen, E. A. Wu, X. Wang, A. Banerjee and Y. S. Meng, *J. Mater. Chem. A*, 2020, **8**, 5049–5055.
35 W. Yan, Z. Mu, Z. Wang, Y. Huang, D. Wu, P. Lu, J. Lu, J. Xu, Y. Wu, T. Ma, M. Yang, X. Zhu, Y. Xia, S. Shi, L. Chen, H. Li and F. Wu, *Nat. Energy*, 2023, **8**, 800–813.
36 P. N. Le Pham, M. A. Kraft and W. G. Zeier, *ACS Appl. Mater. Interfaces*, 2025, **17**, 12261–12270.
37 S. Ohno, T. Bernges, J. Buchheim, M. Duchardt, A.-K. Hatz, M. A. Kraft, H. Kwak, A. L. Santhosha, Z. Liu, N. Minafra, F. Tsuji, A. Sakuda, R. Schlem, S. Xiong, Z. Zhang, P. Adelhelm, H. Chen, A. Hayashi, Y. S. Jung, B. V. Lotsch, B. Roling, N. M. Vargas-Barbosa and W. G. Zeier, *ACS Energy Lett.*, 2020, **5**, 910–915.
38 L. Imholt, T. S. Dörr, P. Zhang, L. Ibing, I. Cekic-Laskovic, M. Winter and G. Brunklaus, *J. Power Sources*, 2019, **409**, 148–158.
39 W. Zhang, D. A. Weber, H. Weigand, T. Arlt, I. Manke, D. Schröder, R. Koerver, T. Leichtweiss, P. Hartmann, W. G. Zeier and J. Janek, *ACS Appl. Mater. Interfaces*, 2017, **9**, 17835–17845.